2016

Steady State and Transient Computational Study of Multiple Hydrokinetic Turbines

Cosan Daskiran
Lehigh University

Steady State and Transient Computational Study of

Multiple Hydrokinetic Turbines

By

Cosan Daskiran

A Thesis

Presented to the Graduate and Research Committee

Of Lehigh University

in Candidacy for the Degree of Master of Science

in

Mechanical Engineering

Lehigh University

May 2016

This thesis is accepted and approved in partial fulfillment of the requirements for the

Master of Science degree in Mechanical Engineering

_____

Date Approved

_____

Dr. Alparslan Oztekin

Thesis Advisor

_____

Dr. D. Gary Harlow, Chairperson

Mechanical Engineering and Mechanics

iii

Table of Contents

List of Tables

List of Figures

Acknowledgements

The author would first like to express his appreciation to his advisor, Professor Alparslan Oztekin for his continued guidance, motivation and encouragement. The author would also want to thank Dr. William Chris Schleicher and Dr. Jacob Riglin for their help with the CFD study of hydrokinetic turbines. Additionally, the author would like to express his sincerest appreciation to his sponsor, Turkish Military Academy. Finally, the author wishes to express his appreciation to his wife Burcu, parents Erol and Aynur, and his sister Merve for their continued motivation and help in the preparation of this thesis.

Nomenclature

Full Scripts

C	coefficient
D	diameter, m
$F_{1,2}$	blending function
GCI	grid convergence index, %
k	turbulent kinetic energy, J/kg
m	meridional length, m
P	power, W
p	pressure, Pa
Re	Reynolds number
S	mean rate-of-strain tensor, 1/s
t	time, s
U	velocity, m/s
w	domain boundary
X	distance in x-direction, m
Y	distance in y-direction, m
Z	distance in z-direction, m
C	coefficient
D	diameter, m

Greek Symbols

α, β, σ	closure coefficients
β	relative angle, $^\circ$
β^*	constant, 0.09
τ_{ij}	Reynolds Stress Tensor, Pa
δ_{ij}	Kronecker delta function
μ_t	Turbulent Dynamic Viscosity, Pa.s
Δ	change in variable
ε	turbulent dissipation rate, m^2/s^3
ϵ	permutation symbol
λ	tip-speed ratio
θ	wrap angle, $^\circ$
μ	dynamic viscosity, Pa.s
v	kinematic viscosity, m^2/s
ρ	density, kg/m^3
ω	specific dissipation rate, 1/s
Ω	Angular velocity, 1/s

Superscript

*	denotes a closure coefficient
'	denotes the blade angle

Subscripts

A	single unit
a	absolute

ix

H	hydraulic
h	at the hub
i,j,l,q,s,t	tensor indices
max	maximum value
r	rotating reference frame
t	at the tip
x	at x-direction
y	at y-direction
z	at z-direction
∞	free stream
1,2	variable indicator

ABSTRACT

Computational fluid dynamics (CFD) simulations have been conducted for different configurations of pre-designed multiple hydrokinetic turbines. The turbines are modeled physically within the fluid domain instead of low fidelity actuator lines or actuator disk modeling approaches. The turbulence model, k-ω Shear Stress Transport (SST) was employed to resolve turbulent flow field. The primary focus of this study is to investigate transient behavior of multiple turbines and providing solutions to enhance downstream turbine performance in close proximity to the upstream turbine wake. The wake interaction behind the upstream turbine reduces downstream turbine performance with inline configurations being the most severe cases. One of the many suggested solutions is staggering downstream units beyond the wake region. Other solutions for an inline array: increasing the longitudinal distance between units and modifying downstream turbine rotation speed to move turbine operation point to the best efficiency point.

The CFD simulations revealed that the upstream turbine power generation is nearly the same with the single unit power generation for each multiple turbine arrangement. The downstream turbine relative power obtained was 0.18 for the unit placed inline and 0.98 when it was placed outside the wake region. For inline configurations, increasing the stream-wise spacing between the units from $6D_t$ to $10D_t$ improved relative power from 0.16 to 0.60, while reducing the rotation speed from 150 rpm to 100 rpm resulted relative power increment from 0.24 to 0.55.

1

1. INTRODUCTION

1.1 Motivation

Conventional hydropower is one of the most primary renewable energy sources as a result of natural water cycle. Hydropower produces clean energy whereas fossil fuels spread out several harmful gases which have a substantial influence on global warming. Conventional hydropower generates almost 78 GW of power per year, which forms more than half of U.S. renewable energy generating capacity [1]. However, conventional hydropower needs dams to meet the required hydraulic head and flow rate for large body of water. These civil constructions require high initial cost and cause degradation on surrounding areas and aquatic ecosystems.

Kinetic energy of natural streams drives hydrokinetic turbine rotor, reducing necessary civil constructions and costs for power production. The theoretically recoverable hydrokinetic energy estimation in continental USA is approximately 1,381 TWh per year [2]. Hydrokinetic turbines have the same principle as wind turbines which extract kinetic energy of moving air for electricity generation. The water density is almost three order of magnitude (nearly 832 times) higher than the air density; however micro-hydrokinetic turbine energy generation capacity is generally lower than that of wind turbines due to restrictions in both unit size and flow speed. According to United States Geological Survey (USGS), 51% of the rivers in United States have free stream velocity magnitude varying between 0.75 m/s and 2.5 m/s which is appropriate for micro-hydrokinetic turbine applications [3] while wind turbines operates with one order of

magnitude higher free stream velocities. Rotor diameter size in micro-hydrokinetic turbine designs are limited by river and current depths. Due to lower free stream velocity and small-scale turbine geometry for micro-hydrokinetic turbines, multiple unit operation becomes indispensable to increase power output.

1.2. Literature Review

Various experimental, numerical and analytical studies have been carried out so far highlighting efforts to improve power generation in multi-unit configurations. The turbine geometry is generally modeled by using actuator line model, actuator disk theory, or blade element momentum (BEM) theory for simplification instead of real turbine geometry. In the body of the present work, pre-designed physical turbine geometries were modeled numerically for specified unit configurations and arrays.

Jo *et al.* [4] has studied different configurations of multiple hydrokinetic turbines experimentally and numerically by modeling the turbine geometry as actuator disk. They studied two inline turbines (axial) with $1D_t$ stream-wise spacing and two side by side turbines (transverse) with $D_t/2$ lateral spacing between turbine rotor tips and concluded that the transverse configuration does not have much effect on turbines' performance while downstream turbine in axial configuration undergoes significant performance decline. Malki *et al.* [5] applied coupled blade element momentum (BEM) – CFD model to carry out simulations for several configurations of tidal turbines. They concluded that downstream turbine performance increases by longitudinal spacing between two turbines aligned within the stream-wise direction. They also concluded that the increase in

3

transverse spacing between two turbines accelerate the flow velocity between turbines which suggests placing third turbine between two turbines within a longitudinal spacing is advantageous.

Mycek *et al.* [6] conducted experiments for three-bladed horizontal axis turbines modeled with NACA 63418 profile data. They carried out the experiments for different values of stream-wise spacing among turbines. They provided downstream turbine power coefficient and thrust coefficient based on free stream velocity as a function of tip-speed ratio and the results showed that the increase in longitudinal spacing provides enhanced turbine performance output for downstream turbine. Gebreslassie *et al.* [7] compared analytical and numerical design of wake interactions for multiple turbines modeled as actuator disks. They concluded that when the axial spacing between two turbines is $20D_t$, the downstream turbine performance recovers to 91% of single unit output.

Churchfield *et al.* [8] conducted Large Eddy Simulations (LES) for different configurations of multiple tidal turbines modeled as actuator lines to take tip vortices into consideration. They observed an increase in velocity between the units placed side by side as a result of mass conservation. This observation suggested staggered configuration of turbines for optimum power output.

In this study, multiple inline and staggered configurations of pre-designed [9] two-bladed micro-hydrokinetic turbine rotor performance has been investigated using CFD tools. The three-bladed version of the turbine was optimized by Schleicher [10] and validated experimentally by Riglin *et al.* [11, 12, 13] within relative error less than 3.0%

4

at turbine optimum design point. The main goal of this study was to determine transient effects in the flow field and turbine performance for both inline and staggered configurations of two identical turbines. The second goal is to increase inline-downstream turbine performance. In addition to inline/staggered configuration, more steady-state simulations are conducted for inline configuration to improve downstream unit performance through altering longitudinal distance between units and the rotation speed observed by the downstream unit.

2. GEOMETRY AND MESHING

2.1 Turbine Geometry and Computational Domain

The two-bladed actual micro-hydrokinetic turbine rotor geometry provided by Schleicher *et al.* [9] was used for multi turbine CFD computations. The turbine rotor is designed within high solidity of 0.83, and the maximum power coefficient of 0.43, equivalent to 73.7% of the Betz limit. Schleicher *et al.* [9] designed the turbine rotor to obtain 500 Watts of power output with service conditions: 2.25 m/s of free stream velocity and 15.708 rad/s of angular rotor speed in clockwise direction. The turbine rotor design variables are hub diameter (D_h) of 0.0635 m., turbine tip diameter (D_t) of 0.5334 m., turbine blade thickness of 0.0127 m., the meridional blade length (Δm) of 0.1488 m. (the axial distance from blade leading edge to blade trailing edge), wrap angle ($\Delta\theta$) of 142.29°, relative flow angle (β) of 52.58° and relative blade angle (β') of 72.26°. The front view and top view of turbine rotor geometry are depicted in Figure 1.
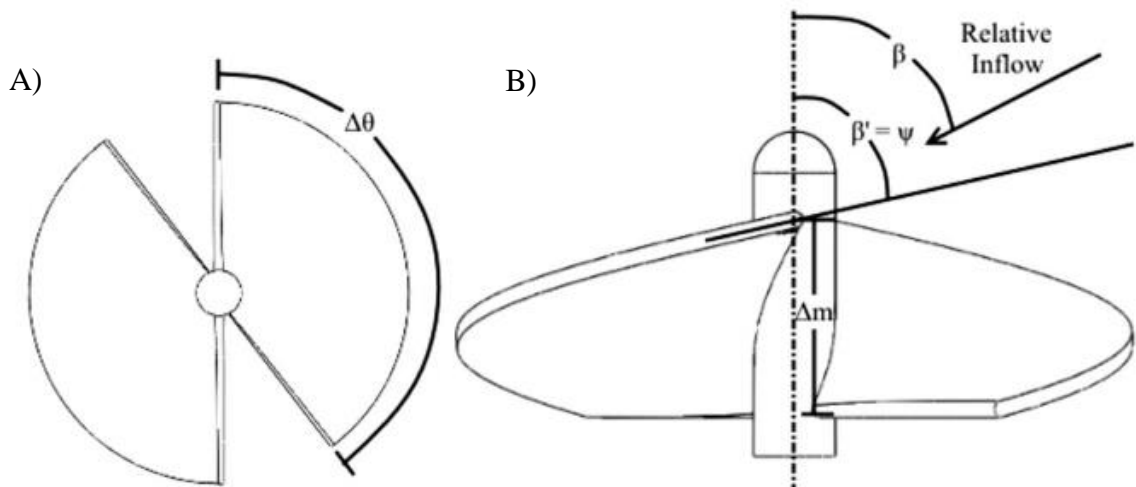
Figure 1. Turbine rotor A) front and B) top view [9]

The computation domains for both staggered and inline placements involve subdomains for river and turbine regions. The river subdomain is stationary whereas the turbine subdomains are rotating with a specified rotation rate. The river domain length for both configurations is $21.71D_t$, however the river domain width is $15.14D_t$ for inline and $12.38D_t$ for staggered unit arrangements. The longitudinal spacing among the units is $6D_t$ for each configuration and the lateral spacing between the turbine rotors is $0.7D_t$ from blade tip to blade tip in staggered placement.

The computational domain boundaries influence turbine performance results when they are in close proximity to the studied unit. The computational domains and boundaries utilized for both configurations are observed in Figure 2 and Figure 3. The upstream turbine is located $5.71D_t$ away from the uniform velocity-inlet boundary to provide fully developed turbulent flow entrance to the upstream turbine. The spacing between downstream turbine leading edge and outlet boundary is $10D_t$. The boundary condition for river bottom surface and top surface is no-slip wall and free-slip wall respectively. The free slip wall produces an artificial free surface, mimicking the surface of a river.

The turbine domain is a circular rotating domain inside the stationary river domain. The turbine domain diameter, $1.5D_t$, is large enough to include wake and tip vortices in the rotating turbine region, decreasing the interpolation error occurring at the interface between rotating and stationary domains. The distance between turbine subdomain inlet and upstream turbine leading edge is $3.52D_t$ and $2.57D_t$ for inline and

staggered placements respectively. The turbine subdomain outlet is placed within $7.14D_t$

distance from downstream turbine leading edge for both turbine settlements.
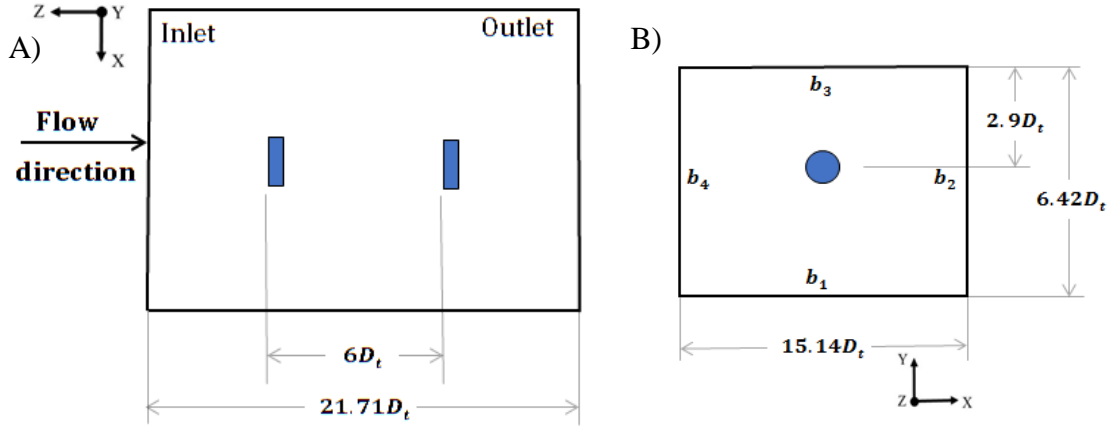
Figure 2. The inline turbine placement A) top view and B) front view with normalized dimensions in reference to turbine tip diameter ($\boldsymbol{D_t}$)
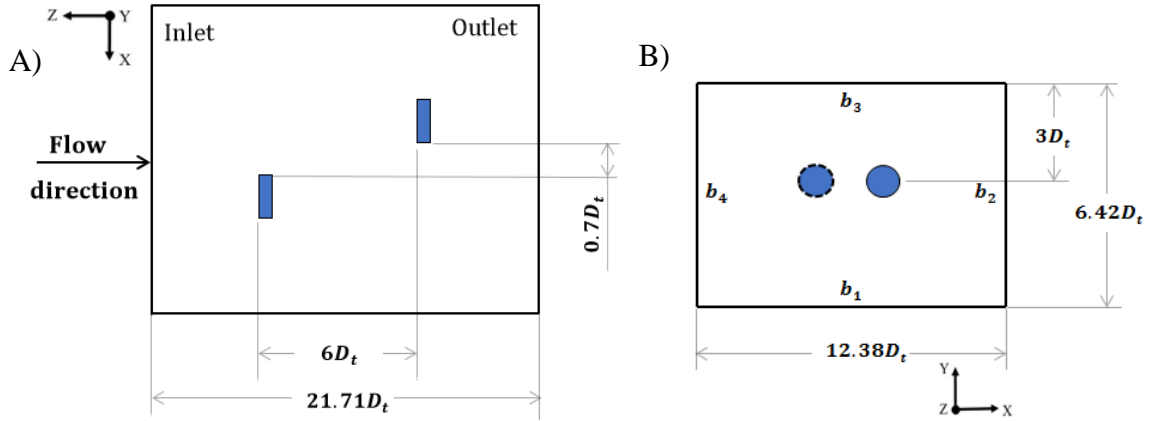
Figure 3. The staggered turbine placement A) top view and B) front view with normalized dimensions in reference to turbine tip diameter ($\boldsymbol{D_t}$).

2.2 Meshing

Meshing the computational domain with orthogonal, high-quality cells is vital for

producing accurate results. The turbine and river subdomains are meshed separately and

connected to each other by defining interfaces among the connecting surfaces. Due to the

8

refined mesh in turbine subdomain, the nodes are not aligned perfectly on the interfaces existing between the stationary and rotating domains. Therefore, General Grid Interface (GGI) mesh connection method is implemented to interpolate variables among the domains. The accuracy of CFD simulation is dependent on the alignment of the nodes. GGI method needs more computation resources than that of one-to-one mesh connection method [14].

Hexahedral cells are used to generate a completely structured grid. The structural mesh has several benefits over unstructured tetrahedral mesh elements. The structured mesh provides a uniform well-organized pattern in the domain while unstructured mesh connects triangular mesh elements non-uniformly in the domain. The structured mesh which is arranged within the flow direction provides more reliable results and reduces the discretization error.

The river domain and turbine domains are meshed by using ANSYS-Meshing module and ANSYS-TurboGrid, respectively. TurboGrid accomplishes structured mesh for curved shapes specifically for turbomachinery related applications. The mesh along the turbine blade is refined for leading edge and trailing edge and tip of the blade to capture the boundary layer or flow seperation resulting along the blade geometry during unit operation. The mesh at the inlet for both staggered and inline configurations, the mesh along the turbine rotor and hub, and the mesh present at the blade tip are depicted in the Figures below:

9
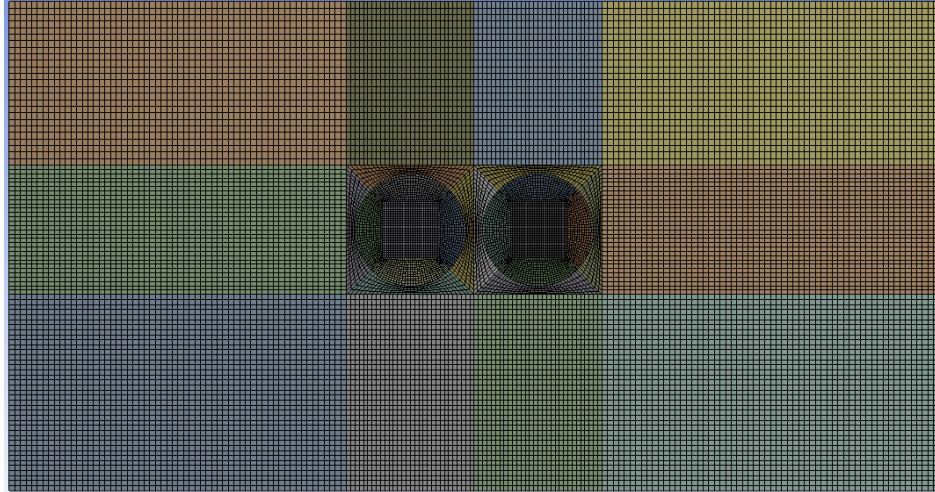
Figure 4. The mesh on the inlet for staggered placement
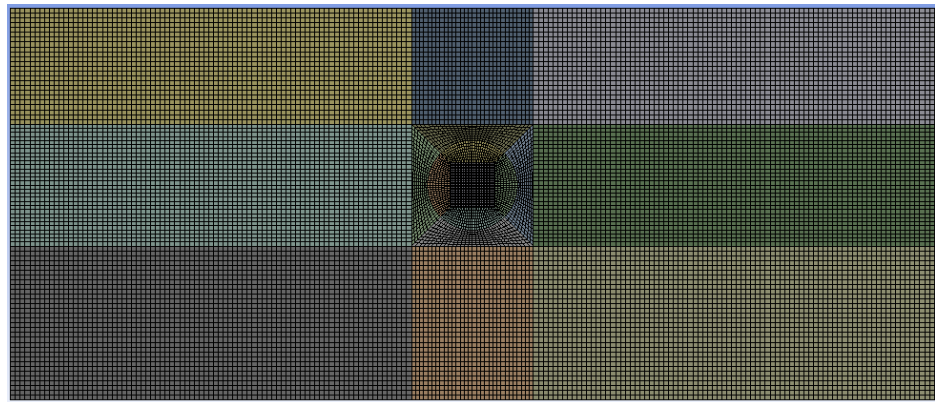
Figure 5. The mesh on the inlet for inline placement

A)

B)
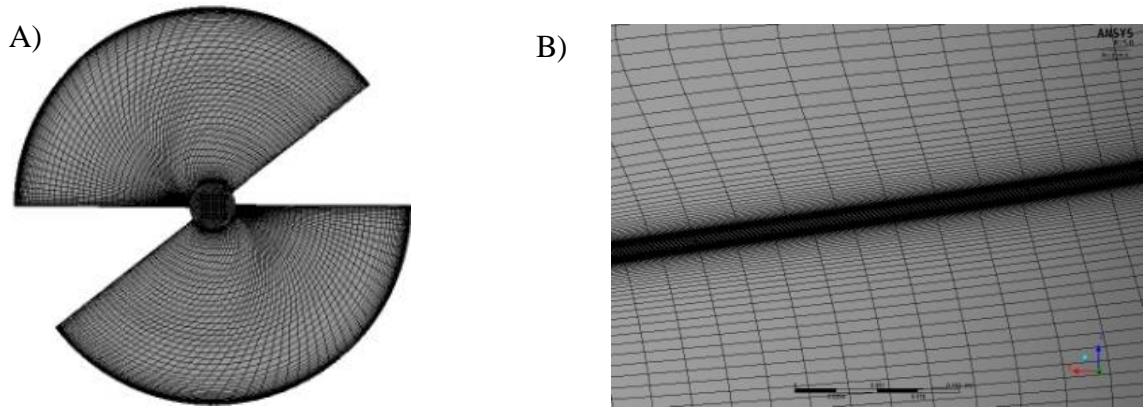
Figure 6. The mesh on A) blade rotor and hub, B) blade tip

3. MATHEMATICAL AND NUMERICAL MODELING

3.1. Conservation of Mass and Momentum

In this section, the Reynolds Averaged Navier Stokes equation is derived for absolute reference frame assuming incompressible flow and constant density. The mass and momentum equations are modified for rotating frame of reference by inserting acceleration terms, centrifugal and Coriolis forces into the governing equations. In the derivation process, the velocity is separated into two components as fluctuating component ($u'(x_i, t)$) and time-averaged component ($\bar{u}(x_i)$) as shown in equation (1).

$$u(x_i, t) = \bar{u}(x_i) + u'(x_i, t) \qquad u'(x_i, t) = \lim_{T \to \infty} \frac{1}{T} \int_{t}^{t+T} u(x_i, t)dt \qquad (1)$$

3.1.1. Absolute Frame of Reference

The first step in the derivation is substituting $u(x_i, t)$ into mass and momentum conservation equations shown in equations (2) and (3) in continuous medium.

$$\frac{\partial u_i}{\partial x_i} = 0 \qquad (2)$$

$$\frac{\partial u_i}{\partial t} + u_j \frac{\partial u_i}{\partial x_j} = -\frac{1}{\rho} \frac{\partial p}{\partial x_i} + v \frac{\partial^2 u_i}{\partial x_j \partial x_j} \qquad (3)$$

The substation of equation (1) into equations (2) and (3) results in the modified equations (4) and (5) shown below.

$$\frac{\partial \bar{u}_i}{\partial x_i} + \frac{\partial u_i'}{\partial x_i} = 0 \tag{4}$$

$$\frac{\partial(\bar{u}_i + u_i')}{\partial t} + \bar{u}_j \frac{\partial \bar{u}_i}{\partial x_j} + \bar{u}_j \frac{\partial u_i'}{\partial x_j} + u_j' \frac{\partial \bar{u}_i}{\partial x_j} + u_j' \frac{\partial u_i'}{\partial x_j}$$

$$= -\frac{1}{\rho} \frac{\partial(\bar{p} + p')}{\partial x_i} + \nu \frac{\partial^2(\bar{u}_i + u_i')}{\partial x_j \partial x_j} \tag{5}$$

After some rearrangements, the final form of the time averaged continuity and Navier Stokes equation are obtained as follows. (Note that $\overline{u_i'} = 0$ and $\bar{\bar{u}}_i = \bar{u}_i$)

$$\frac{\partial \bar{u}_i}{\partial x_i} = 0 \tag{6}$$

$$\frac{\partial \bar{u}_i}{\partial t} + \frac{\partial(\bar{u}_j \bar{u}_i)}{\partial x_j} + \frac{\partial(\overline{u_j' u_j'})}{\partial x_j} = -\frac{1}{\rho} \frac{\partial \bar{p}}{\partial x_i} + \nu \frac{\partial^2 \bar{u}_i}{\partial x_j \partial x_j} \tag{7}$$

The derived equations are similar to equations (2) and (3), except for $\overline{u_j' u_j'}$ term in momentum equation which will be obtained by turbulence modeling equations.

3.1.2. Relative Frame of Reference

Multi Reference Frame (MRF) approach is applied for steady state simulations to take turbine rotation effect into consideration. In this approach, the flow field in unsteady inertial frame is converted to steady non-inertial frame.

$$\frac{\partial U_{r,i}}{\partial x_i} = 0 \tag{8}$$

$$\frac{\partial U_{r,i}}{\partial t} + U_{r,j}\frac{\partial U_{r,i}}{\partial x_j} = -\frac{1}{\rho}\frac{\partial p}{\partial x_j} - 2\epsilon_{ilq}\Omega_l U_{r,q} - \epsilon_{ilq}\epsilon_{qst}\Omega_l\Omega_s x_t + \nu\frac{\partial^2 U_{r,i}}{\partial x_l \partial x_l} \tag{9}$$

In these equations, U_r is the velocity in the rotating reference frame, Ω is angular speed of rotating frame, p is static pressure, ρ is fluid density, ϵ is the permutation symbol and j, l, q, s, and t are index placeholders. Similar substitution can be applied for equations (8) and (9) to obtain conservation equations in Reynolds averaged form.

MRF approach solving conservation equations in relative frame of reference is a simpler technique for steady state rotating machinery simulations compared to the Transient Rotor Stator approach used for transient simulations with the conservation equations in absolute frame.

3.2. Turbulence Modeling

Mendel's k-ω Shear Stress Transport (SST) [15, 16] turbulence model is a two-equation eddy-viscosity turbulence model and is applied for many turbulent flow applications where adverse pressure gradients and wall boundaries are present. This model combines standard k-ω model, which is preferred to predict turbulence near-wall region, and k-ϵ model, which is preferred for free stream flows. The k-ω and k-ϵ turbulence models are two equation popular models and offers reliable results for Computational Fluid Dynamics applications. The k-ω SST model uses the advantage of k-ω turbulence model close to the walls to predict flow separation and behaves like k-ϵ model in free stream to predict wakes and circulation properly. Blending functions, F, are implemented to allow for the transition in model behavior. The two equation model for turbulent kinetic energy and specific dissipation rate are given by the following equations [16, 17]

$$\frac{\partial(\rho k)}{\partial t} + \frac{\partial(\rho u_j k)}{\partial x_j} = \tau_{ij}\frac{\partial u_i}{\partial x_j} - \beta^*\rho\omega k + \frac{\partial}{\partial x_j}\left[(\mu + \sigma_k \mu_t)\frac{\partial k}{\partial x_j}\right] \qquad (10)$$

$$\frac{\partial(\rho\omega)}{\partial t} + \frac{\partial(\rho u_j \omega)}{\partial x_j} = \frac{\rho\gamma}{\mu_t}\tau_{ij}\frac{\partial u_i}{\partial x_j} - \beta\rho\omega^2 + \frac{\partial}{\partial x_j}\left[(\mu + \sigma_\omega \mu_t)\frac{\partial\omega}{\partial x_j}\right] \qquad (11)$$
$$+ 2(1 - F_1)\frac{\rho\sigma_{\omega 2}}{\omega}\frac{\partial k}{\partial x_j}\frac{\partial\omega}{\partial x_j}$$

The Reynold's Stress Tensor, τ_{ij}, is defined as:

$$\tau_{ij} = \mu_t \left(\frac{\partial u_i}{\partial x_j} + \frac{\partial u_j}{\partial x_i} - \frac{2}{3} \frac{\partial u_k}{\partial x_k} \delta_{ij} \right) - \frac{2}{3} \rho k \delta_{ij} \tag{12}$$

With turbulent dynamic viscosity defined as $\mu_t = \frac{\rho a_1 k}{\max(a_1 \omega; F_2 S)}$ and blending functions provided below:

$$F_2 = \tanh(max \left[2 \frac{\sqrt{k}}{\beta^* \omega y}; \frac{500v}{y^2 \omega} \right]^2) \tag{13}$$

$$CD_{kw} = \max \left(\frac{2\rho \sigma_{\omega 2}}{\omega} \frac{\partial k}{\partial x_j} \frac{\partial \omega}{\partial x_j}; \ 10^{-20} \right) \tag{14}$$

$$F_1 = \tanh(min \left[\max \left(\frac{\sqrt{k}}{\beta^* \omega y}; \frac{500v}{y^2 \omega} \right); \frac{4\rho \sigma_{\omega 2} k}{CD_{k\omega} y^2} \right]^4) \tag{15}$$

In these equations, F_1 and F_2 are blending functions, y is the distance to the nearest wall, CD_{kw} cross diffusion term of the equation for specific dissipation rate in standard k-ϵ model, S is invariant measure of strain rate. If ϕ_1 depicts any constant in original k-ω model and ϕ_2 represents any constant in standard k-ϵ turbulence model, the value of the same constant (ϕ) in k-ω SST model equations (10) and (11) is calculated by the following relationship

$$\phi = F_1 \phi_1 + (1 - F_1) \phi_2 \tag{16}$$

ϕ_1 represents any constant value shown below for original k-ω model as follows:

$$\sigma_{k1} = 0.85, \quad \sigma_{\omega 1} = 0.5, \quad \beta_1 = 0.0750, \quad \beta^* = 0.09, \quad \kappa = 0.41,$$

15

$$\gamma_1 = \beta_1/\beta^* - \sigma_{\omega 1}\kappa^2/\sqrt{\beta^*}$$

ϕ_2 represents any constant value shown below for standard $k\text{-}\epsilon$ model as follows:

$$\sigma_{k2} = 1, \quad \sigma_{\omega 2} = 0.856, \quad \beta_2 = 0.0828, \quad \beta^* = 0.09, \quad \kappa = 0.41,$$

$$\gamma_2 = \beta_2/\beta^* - \sigma_{\omega 2}\kappa^2/\sqrt{\beta^*}$$

Near-Wall Modeling

No-slip wall boundary condition implies zero velocity for the velocity component parallel to the wall. The zero velocity at wall and the flow velocity at outer part of the wall region result steep velocity gradient near wall region. As a result, viscous effects are dominant in this region. Therefore, the element size normal to the wall must be small enough to resolve the boundary layer accurately. The main goal of present research is to determine flow characteristics around the turbine and accurately predict axial thrust and power output by the turbine. In order to have reliable and accurate numerical simulation results for thrust and power output, a high-resolution grid was necessary near the turbine wall region.

The near wall region is divided into three sub layers as viscous layer, buffer layer and fully turbulent layer. These regions are modeled by using two alternative approaches as "near-wall model approach" or "wall function approach" depicted in Figure 7. In near-wall model approach, viscous layer resolution is provided numerically by using sufficient

16

finer mesh in near-wall region as shown in Figure 7 documented in Fluent Theory Guide [18]. For the second method, viscous layer and buffer layer are modeled by utilizing wall functions without resolving these layers [19]. The first one, near-wall model approach requires higher computation cost than that of wall function approach due to the high resolution grid near wall.
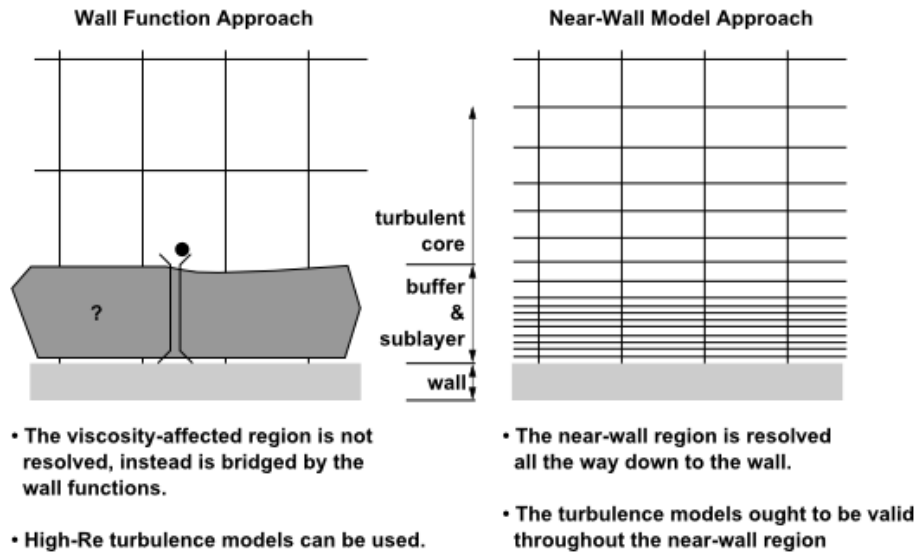
Figure 7. Near wall treatments of two approaches [18]

The quality of near wall resolution can be figured out by the dimensionless wall distance (y^+) value shown below:

$$y^+ = \frac{u_\tau y}{v} \tag{17}$$

where u_τ is the friction velocity ($u_\tau = \sqrt{\tau_w/\rho}$, with τ_w acting as wall shear stress), y is distance to the nearest wall and v is the local kinematic viscosity. The dimensionless wall distance value y^+ is expected in an approximate range of 30 to 300 for wall function

17

approach and 1.0 or lower for near-wall model approach [19]. Attaining $y^+ \sim 1$ for complex 3D geometries is extremely expensive due to the substantial increase in required grid points near wall boundaries. Thus, wall function approach is more applicable because of its computational efficiency.

3.3 Boundary and Initial Conditions

Mathematical models require boundary and initial conditions for solution; at this point the solution of continuity equation and Navier-Stokes equation for computation domain becomes dependent on these conditions specific to the problem studied. In CFD applications, boundary conditions should be assigned for each surface on the fluid domain. The most common boundary conditions are inlet, outlet, wall, periodicity (rotational or translational periodicity) and symmetry.

The present computation domain, boundary conditions utilized are: velocity inlet, pressure –outlet, no-slip wall for river bottom, free-slip wall for river upper surface and translational periodicity for right and left walls in span-wise direction. The uniform velocity inlet is applied with a constant value of 2.25 m/s and the pressure at the outlet is assigned a constant gauge pressure value of 0 Pa. No-slip wall boundary condition implies that tangential velocity component at wall equals to wall velocity and normal velocity is 0. Free-slip wall boundary condition represents no friction between wall and fluid (zero shear stress). The turbine blades and hubs are both no-slip wall rotating with an angular velocity equal to that of the surrounding turbine subdomain region.

Turbulence parameters on the boundaries of inlet and outlet are determined for turbulence kinetic energy (k) and specific dissipation rate (ω) by the following relationships [20]:

$$k = \frac{3}{2}(UI)^2 \qquad\qquad \omega = \frac{\sqrt{k}}{l}(C_\mu)^{\frac{-1}{4}} \qquad\qquad (18)$$

Here U is the average velocity, I is the turbulent intensity, l is the characteristic turbulent length scale, and C_μ is a specified empirical constant. In order to figure out k and ω, the input parameters, turbulent intensity (I) and characteristic length (l) is calculated. Turbulent intensity is determined by the ratio between root-mean-square of velocity fluctuation and average flow velocity as U'/U. The turbulent intensity is estimated by using the following equation:

$$I = 0.16 \, Re_{Dh}^{-1/8} \qquad\qquad (19)$$

Where Re_{Dh} is the Reynolds number based on hydraulic diameter as a characteristic length.

The physical meaning of turbulence length scale (l) is connected to the large eddy size and can be assumed by the equation derived for fully developed duct flows as follows:

$$l = 0.07 \, D_h \qquad\qquad (20)$$

As previously mentioned, transient simulations take longer computation time to determine the resulting flow field. In order to decrease the number of iterations required for each time step convergence, the initial conditions must be applied realistically. The present simulations have been conducted by interpolating steady state result files as an initial condition file for transient simulations. The interpolation of steady results to transient simulation is recommended option for transient simulation because the initial values are already dependent on the flow physics and computational domain boundaries.

4. RESULTS AND DISCUSSION

Schleicher *et al.* [9] has conducted mesh sensitivity analysis for single unit turbine simulation using Grid Convergence Index (GCI) method based on Richardson extrapolation [21, 22, 23, 24]. They compared the thrust and torque outputs for different number of cells, $N_1 = 1,188,542$ cells, $N_2 = 5,929,864$ and $N_3 = 14,607,868$ The relative error between N_1 and N_2 is around 2-3%. This suggests that approximately 12 million cells are acceptable for accurate two-turbine simulation results. In present study, the wake interaction in the region between the units has significant influence on downstream turbine performance. The number of cells used in the present study is higher than the presented value by Schleicher *et al.* [9]. The river and turbine domains for current study are mapped by 4.1 million and 11.1 million elements respectively for inline installment, and 4.0 million and 12.2 million elements respectively for staggered placement.

The element size normal to blade surface is refined to capture the boundary layer. The y^+ value contours are presented in Figure 8. It shows that the y^+ values are in the range for wall function approach and this explains that the meshing is reasonable to capture the boundary layer.

Figure 8. y^+ value on the front surface of A) inline-upstream, B) inline-downstream, C) staggered-upstream and D) staggered-downstream turbine

Time step size is also another significant parameter for transient simulations. The time step size is characterized by non-dimensional number referred to as the Courant–Friedrichs–Lewy (CFL) number. The CFL number must be reduced to values less than 1 (CFL<1) for explicit solvers, however, CFL values up to 5 are acceptable for implicit solvers [25]. The CFL number less than unity means that the fluid travels less than one

cell per time step. The present transient simulations have been accomplished by root mean square (RMS) CFL number 3.53 for inline and 5.14 for staggered configurations. Courant number is determined by:

$$CFL = \frac{u_x \Delta t}{\Delta x} + \frac{u_y \Delta t}{\Delta y} + \frac{u_z \Delta t}{\Delta z} \qquad (21)$$

Here, $u_x, u_y \ and \ u_z$ are components of the velocity, Δt is the time step and Δx, $\Delta y \ and \ \Delta z$ are dimensions of an element in the computational domain.

The time step which generates an acceptable CFL number and accurate transient results for turbine rotation is determined as 0.001 s for both inline and staggered simulations. The specified time step value, 0.001 s, means $0.9^{°}$ rotation of the turbine rotor at each time step for 150 rpm rotation speed. The turbine completes one complete revolution in 0.4 second (400 time steps). The CFL number is depicted in Figure 9 for multiple turbines in inline and staggered configuration for operating conditions: rotation speed of 150 rpm and free stream velocity of 2.25 m/s when longitudinal space is $6D_t$. The CFL number around blade tip, blade leading edge and blade trailing edge is higher than that of other regions on turbine surface. The main reason of high CFL number in aforementioned regions is created finer mesh to capture the boundary layer or flow separation. In addition to finer mesh, the resultant velocity magnitude at turbine blade tip is higher as a result of circumferential speed at blade tip.

23

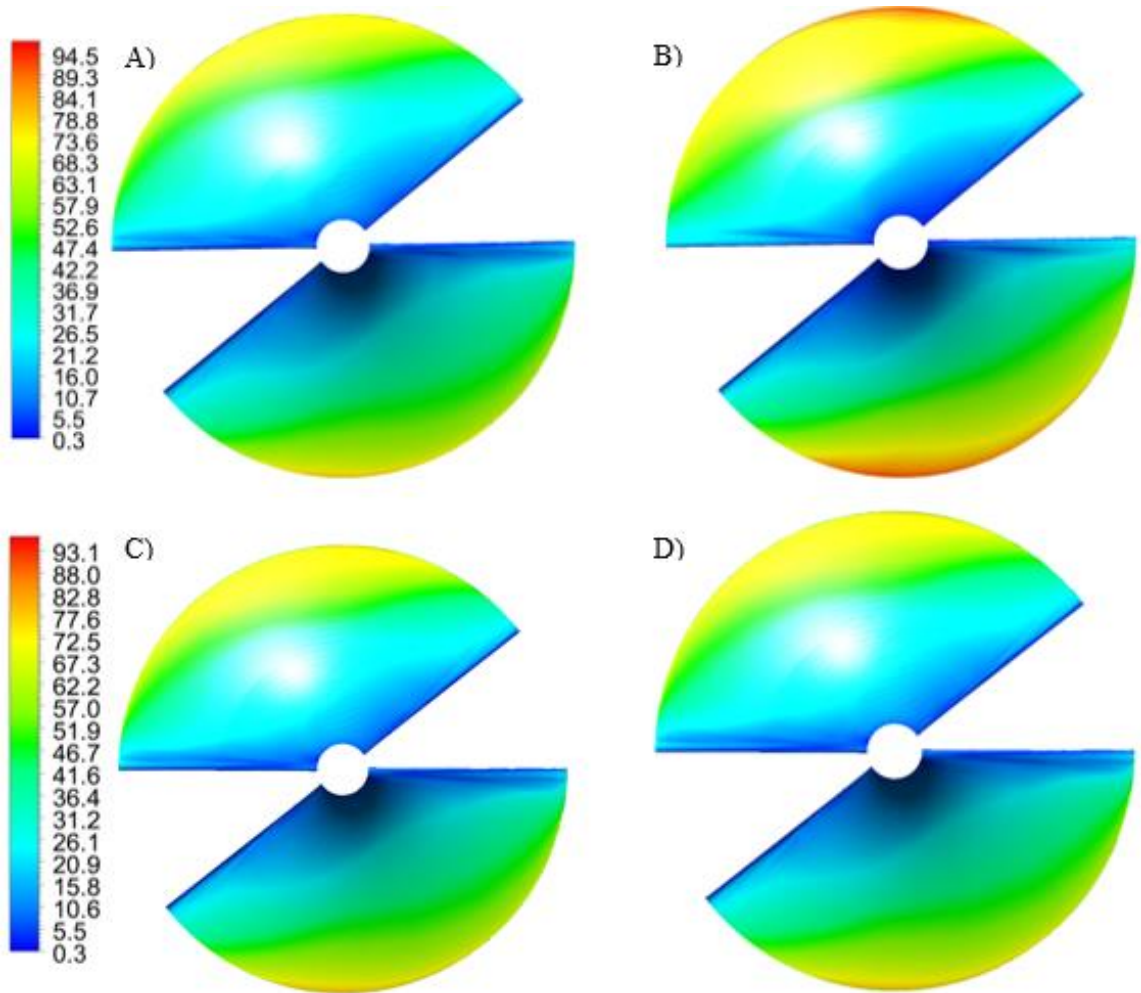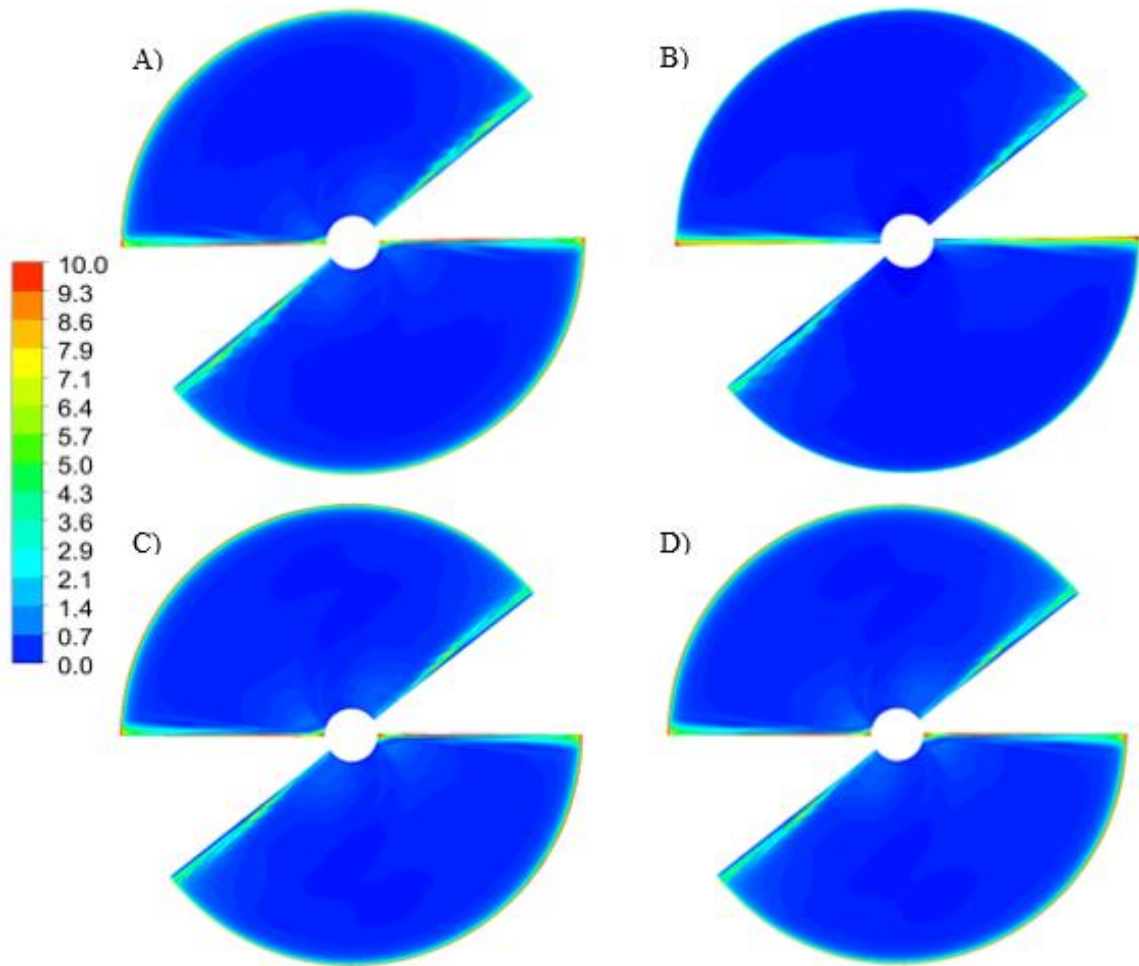Figure 9. CFL number contour on the front surface of A) inline-upstream, B) inline-downstream, C) staggered-upstream and D) staggered-downstream turbine

Flow characterization and blade design can be parameterized by dimensionless tip-speed ratio and Reynolds number. The Reynolds number is the ratio between inertial forces and viscous forces and tip-speed ratio is defined as the ratio between the speed at turbine tip and free stream speed. Equations for the two parameters are shown below:

$$\lambda = \frac{D_t \Omega}{2 U_\infty} \tag{22}$$

$$Re = \frac{\rho U_\infty D_t}{\mu} \tag{23}$$

Here, λ is tip-speed ratio, D_t is turbine tip diameter, Ω is turbine rotation speed, U_∞ is free stream speed, ρ is the fluid density, μ is the fluid dynamic viscosity and Re is the Reynolds number based on turbine tip diameter and $Re \cong 1.9 * 10^6$ for present study.

The performance of the turbines in an array is characterized relative to single unit turbine performance under ideal operation conditions. The non-dimensional parameters for this characterization are power coefficient and relative power, shown below:

$$C_P = \frac{P_A}{\frac{\pi}{8} \rho U_\infty^3 D_t^2} \tag{24}$$

$$\tilde{P} = \frac{P}{P_A} \tag{25}$$

Here C_P is the power coefficient, U_∞ is the average flow speed streaming towards turbine, P_A is the power produced by single unit turbine provided by Schleicher *et al.* [9] under ideal operation conditions, P is the power produced by upstream or downstream turbine, and $\tilde{P}$ is the normalized relative power. The normalized power acts as a ratio between power output of the turbine in the array to the power output of single turbine for the same operating conditions (selected U_∞ and Ω). The fluid speed streaming towards upstream turbine is basically free stream speed, 2.25 m/s. The average fluid speed

25

entering the downstream turbine was determined through a circular area $2D_t$ ahead of the unit. The circular area involves velocity magnitude lower than free stream velocity and its diameter is roughly 0.81 meter for inline/staggered study.

4.1 Inline/Staggered Turbine Performance Comparison

The steady state and transient analysis of two-micro hydrokinetic turbines are performed for inline and staggered array arrangements. The stream-wise spacing between the units for both array arrangements is $6D_t$ and the rotation rate of each turbine is 150 rpm. Different longitudinal spacing and rotation rates were studied by using steady state analysis in Section 4.2 and Section 4.3, respectively.

The relative power and the flow field of each turbine is compared for both steady-state and transient analysis. The relative power of both upstream and downstream turbines in staggered configuration and upstream turbine in inline configuration is approximately unity. This indicates that the units produce almost maximum expected power as predicted by Schleicher *et al.* [9]. However, downstream turbine performs just 18% of single unit turbine within the identical operating conditions. The relative power difference between downstream units in both configurations indicates that the wake interaction behind the upstream turbine causes significant performance reduction for the unit within the wake region during inline placement. The turbine performance is not being affected under staggered unit placement when wake interaction is nonexistent. The average velocity magnitude entering inline-downstream turbine is roughly 1.500 m/s and 1.505 m/s for steady state and transient simulations, respectively.

26

Table 1. Relative Power Results

Unit Arrangement	Transient Solution		Steady-State Solution [26]	
	Upstream Unit	Downstream Unit	Upstream Unit	Downstream Unit
Staggered	0.97	0.97	0.96	0.98
Inline	0.95	0.18	0.96	0.16

The relative error between transient and steady state relative power ranges from 1.03% to 1.05% except for downstream turbine in inline configuration. The relative power deflection of downstream unit in inline placement for steady state simulation shows that steady state approach might not be as capable as transient simulations to predict the wake region behind the upstream turbine, however it is still within the relative error of 11%.

The velocity, pressure and vorticity contours shown in following figures were normalized based on the following equations:

$$\widetilde{U} = \frac{|U_i|}{U} \tag{26}$$

$$\tilde{p} = \frac{p - (-3kPa)}{6kPa - (-3kPa)} \tag{27}$$

$$\widetilde{\Omega} = \frac{\left| \epsilon_{ijk} \frac{\partial U_k}{x_j} \right|}{\Omega} \tag{28}$$

Here, $\widetilde{U}$ is normalized velocity based on the velocity magnitude coming towards turbine (U), $\tilde{p}$ represents normalized pressure and $\widetilde{\Omega}$ is normalized vorticity magnitude based on turbine rotation speed (Ω). Figure 10 through Figure 13 depicts the normalized velocity magnitude $(\widetilde{U})$, the normalized static pressure $(\tilde{p})$ and the normalized vorticity $(\widetilde{\omega})$ for each turbine in both inline and staggered configurations. The left column presents the steady-state results whereas the right column depicts the transient results. The flow fields of both steady and transient analysis show little variance as expected based on the minimal error for predicted power. It is clear from the flow field comparison in Figure 10 through Figure 13 that steady state analysis accurately captures flow field for present hydrokinetic turbine study. The tip vorticity induced by turbine blades results higher velocity and lower pressure regions in the flow field for both steady and transient approaches. The generated vortices breakdown along the longitude region behind the rotor. However, the downstream turbine in inline settlement, Figure 11, does not produce similar tip vortices due to the influence of the wake region induced by upstream turbine. The tip vortices captured by steady state results agree well with that of transient results.
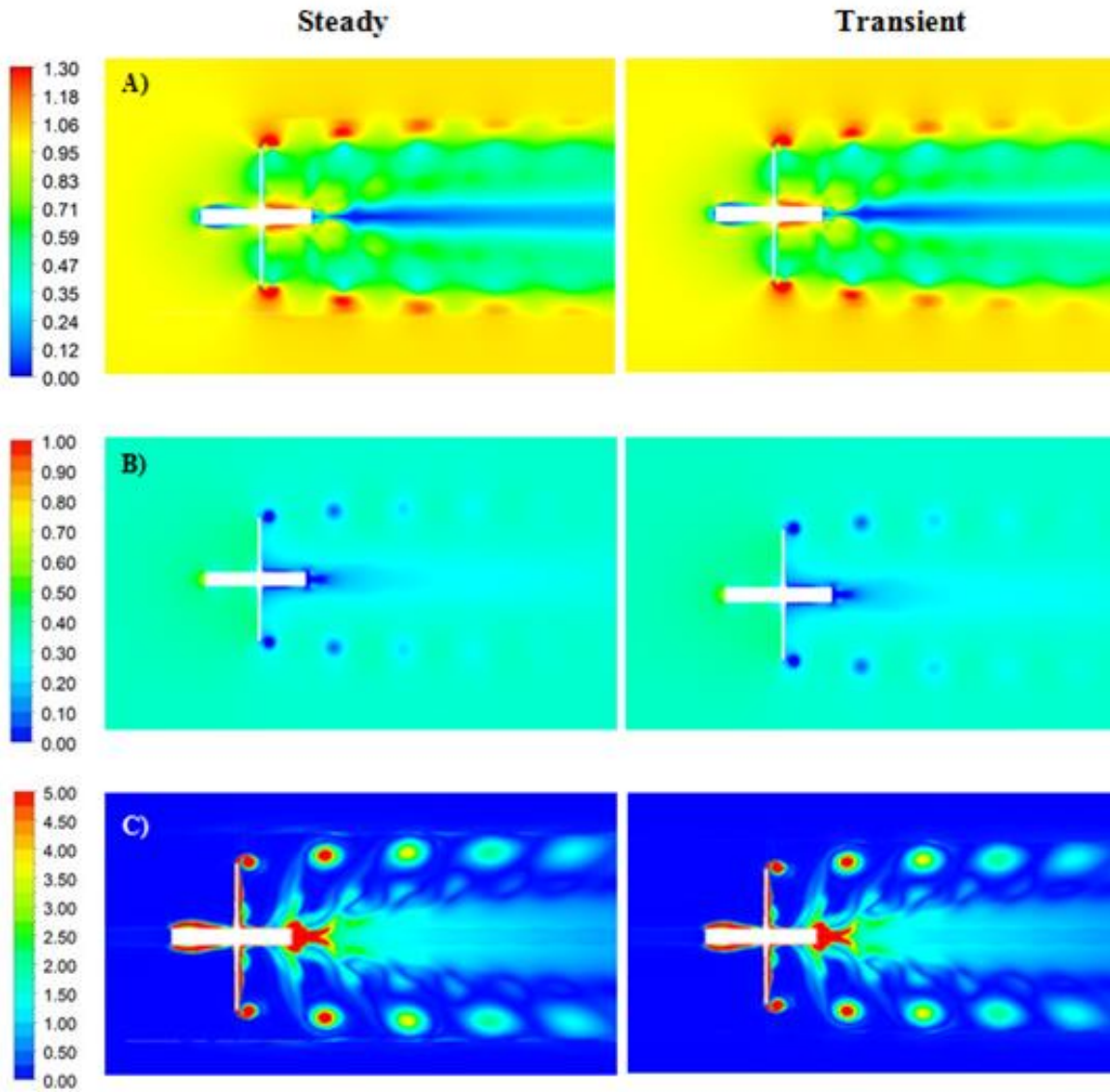
Figure 10. Normalized instantaneous A) velocity, B) pressure, C) vorticity contours of Inline-Upstream turbine for free stream velocity of 2.25m/s and rotation rate of 150 rpm.
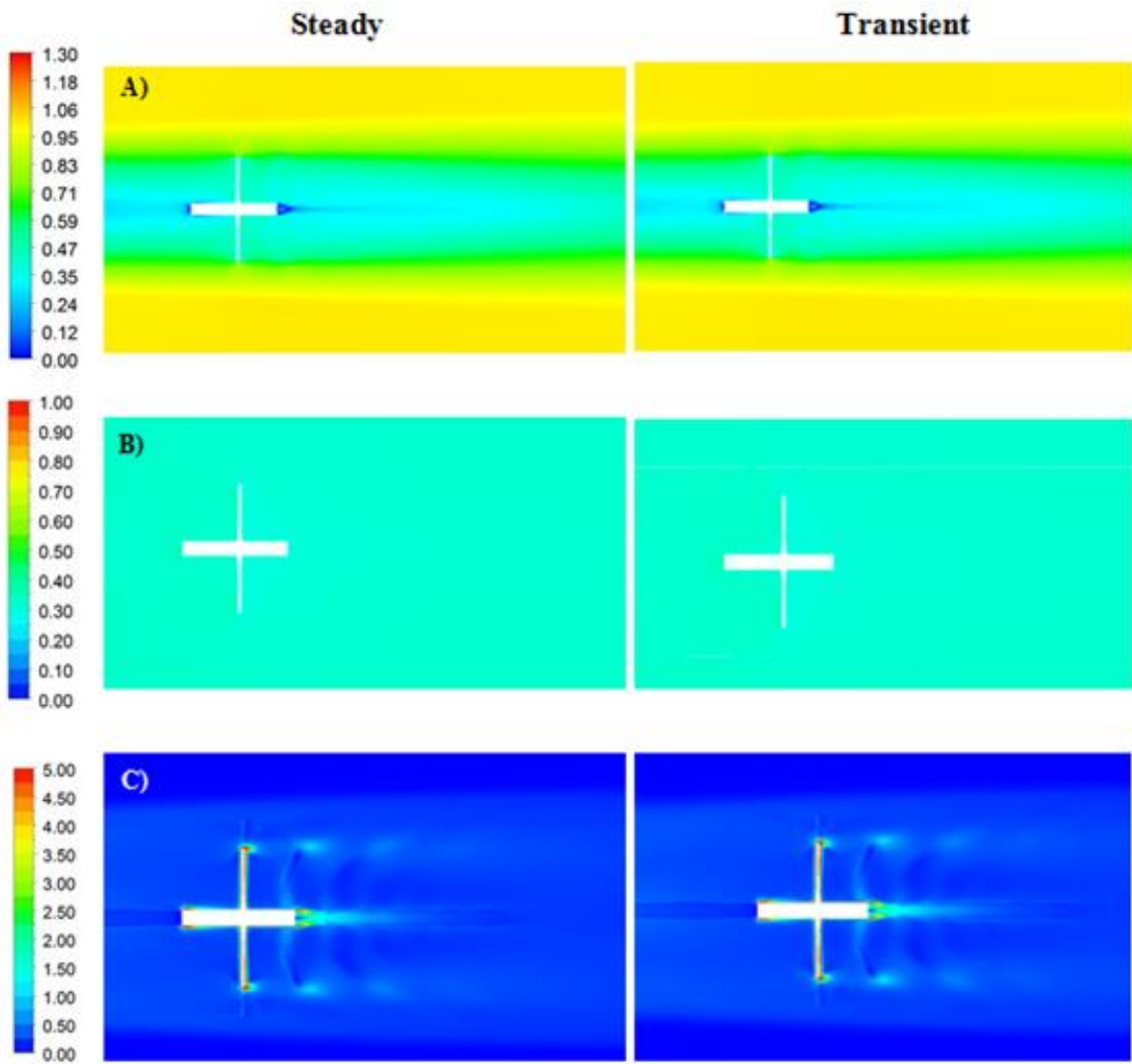
Figure 11. Normalized instantaneous A) velocity, B) pressure, C) vorticity contours of Inline-Downstream turbine for free stream velocity of 2.25m/s and rotation rate of 150 rpm.
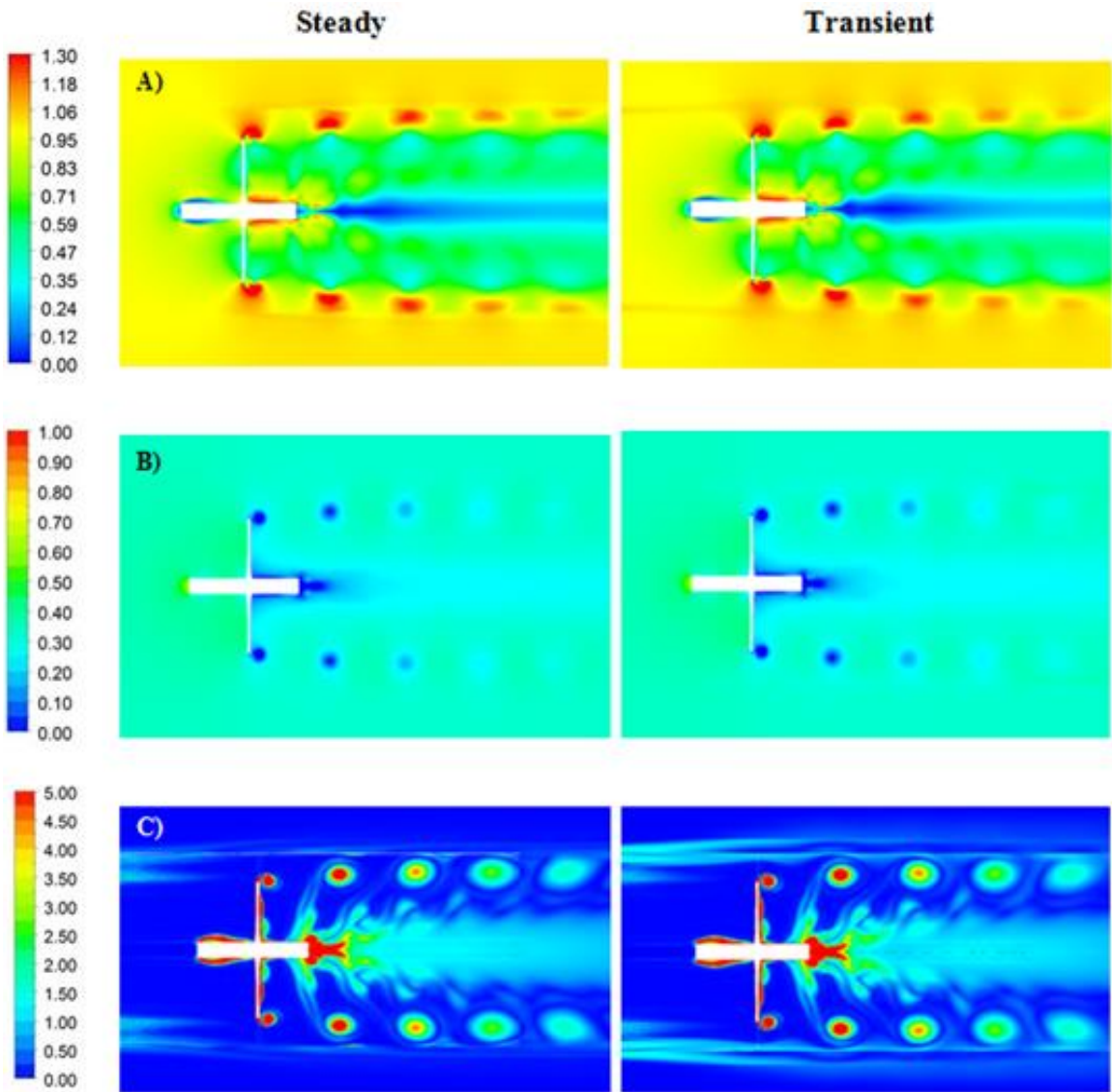
Figure 12. Normalized instantaneous A) velocity, B) pressure, C) vorticity contours of Staggered-Upstream turbine for free stream velocity of 2.25m/s and rotation rate of 150 rpm.

Figure 13. Normalized instantaneous A) velocity, B) pressure, C) vorticity contours of Staggered-Downstream turbine for free stream velocity of 2.25m/s and rotation rate of 150 rpm.
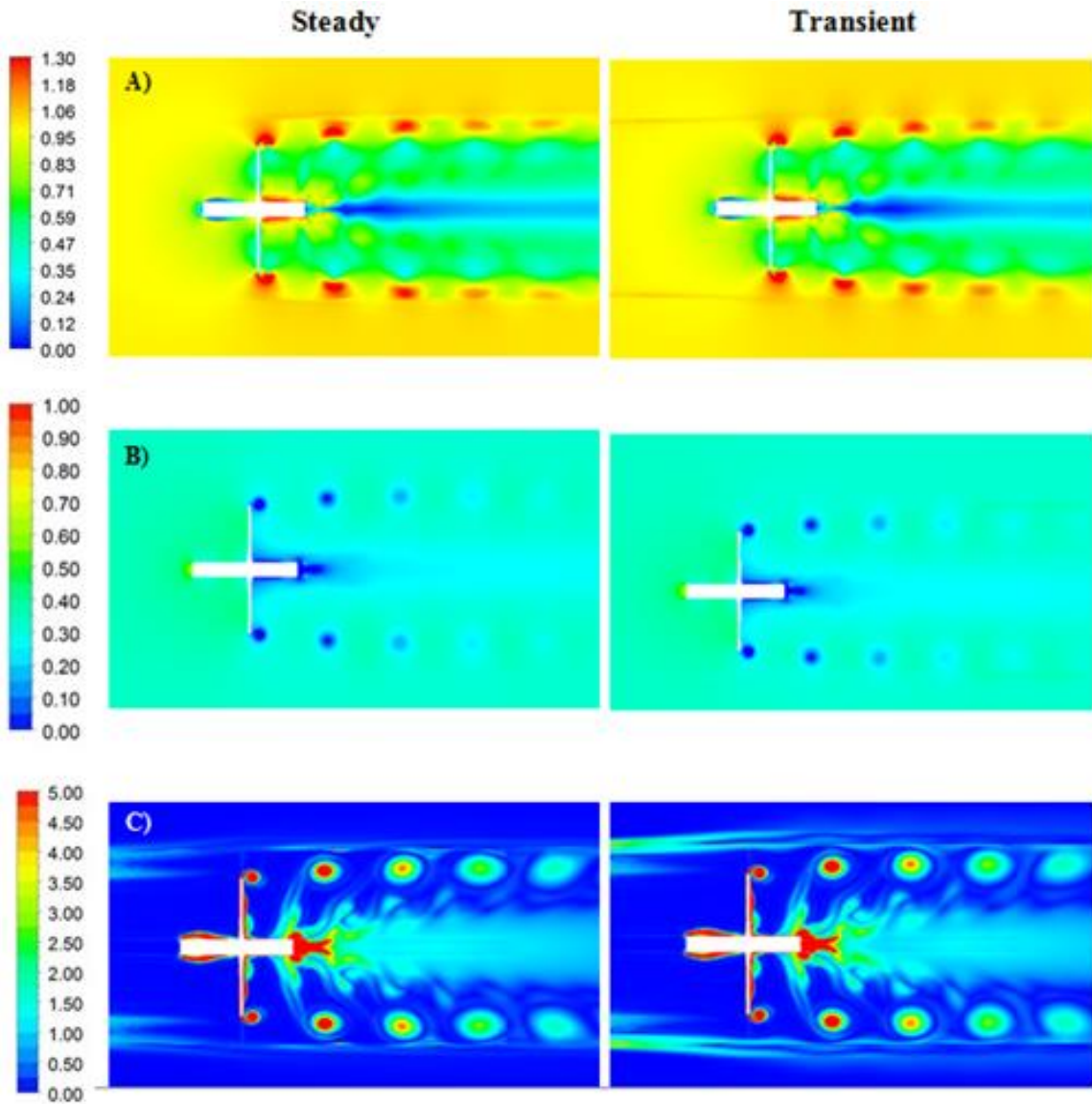
Normalized velocity magnitude shown in Figure 14 compares single unit turbine velocity contours to velocity contours of upstream turbines in staggered and inline arrangements. The preliminary difference between the images is velocity reduction

around the leading region of hub for the turbines in multiple turbine configurations. In addition to velocity reduction around the hub, the flow velocity coming through the turbines arranged as staggered and inline is lower. The observed velocity reduction directly translates to power reduction. Furthermore, the expanding lower velocity region at hub downstream depicts a narrowed velocity region in Figure 14B, while showing permanent expansion in Figure 14A and Figure 14C.
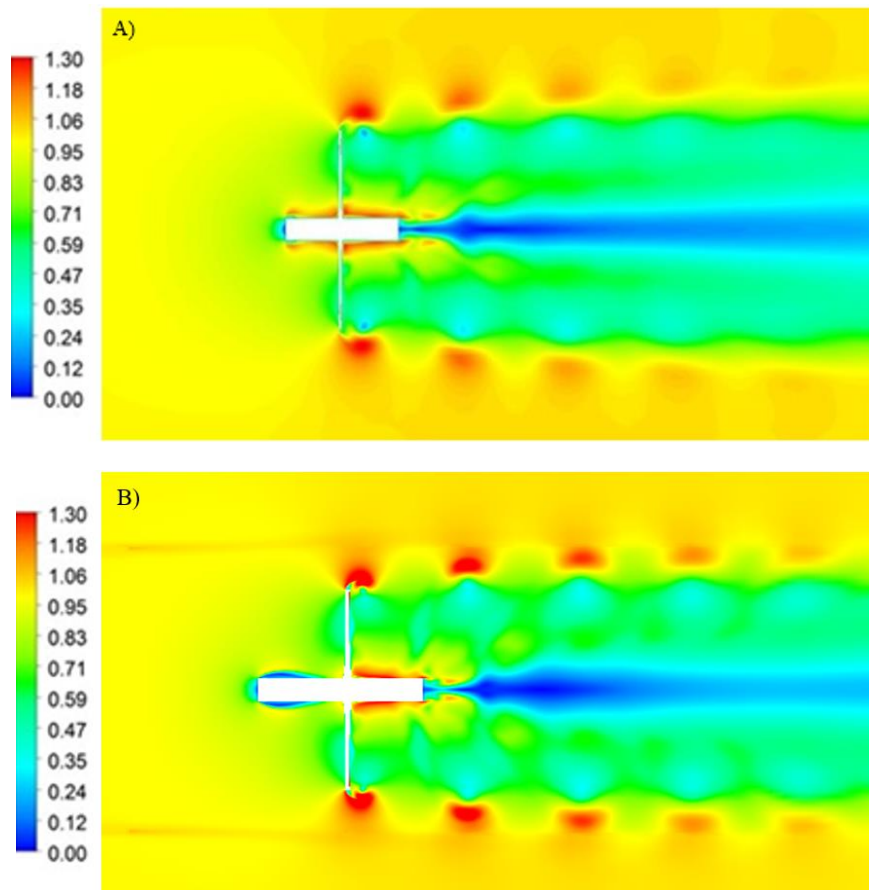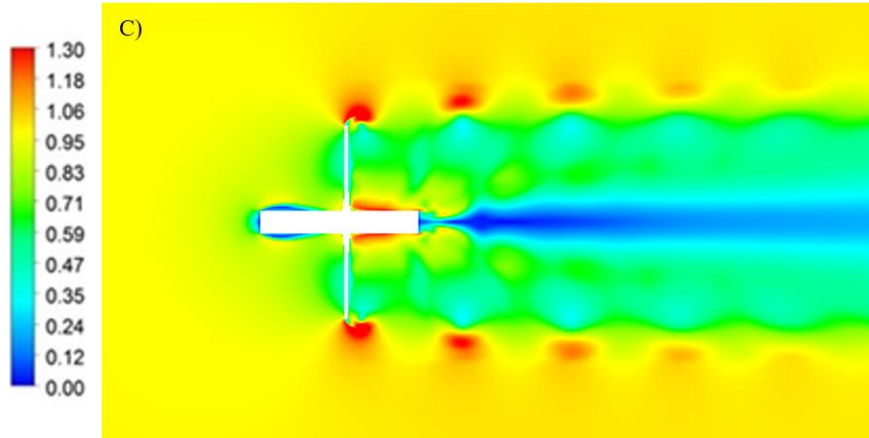
Figure 14. Instantaneous transient normalized velocity contours of A) single unit turbine [27], B) upstream turbine in staggered configuration and C) upstream turbine in inline configuration.

Figure 15A and Figure 15B depict instantaneous normalized velocity contours for downstream units in the staggered and the inline arrangement. The velocity contour for downstream unit in staggered configuration is similar to that of single unit turbine in Figure 14A. The tip vortices generated at the blade tips were not obtained for the inline downstream unit in Figure 15B as a result of chaotic wake entering the downstream unit.

Figure 15. Instantaneous normalized velocity contours for downstream unit in A) staggered and B) inline configuration with free-stream velocity of 2.25 m/s and constant rotation rate of 150 rpm

Figure 16 compares static pressure field for downstream turbine in staggered and inline arrays. Figure 16A shows that the low pressure region occurs at the center of the vortex rope and trailing portion of turbine hub for the staggered case as observed for single turbine analysis in Figure 6B. Figure 16B emphasizes almost constant pressure magnitude around downstream unit and nonexistent tip vortices as the turbines are inline. Figure 17 emphasizes the vorticity magnitude reduction for the inline-downstream case.

35

The staggered-downstream turbine in Figure 17A performs almost same vorticity magnitude as single unit results. However, inline-downstream turbine in Figure 17B depicts tip vorticity breakdown although the incoming flow is chaotic. The maximum vorticity magnitude in helicoidal vortex rope region for inline settlement is 30-40% less than that of staggered one.
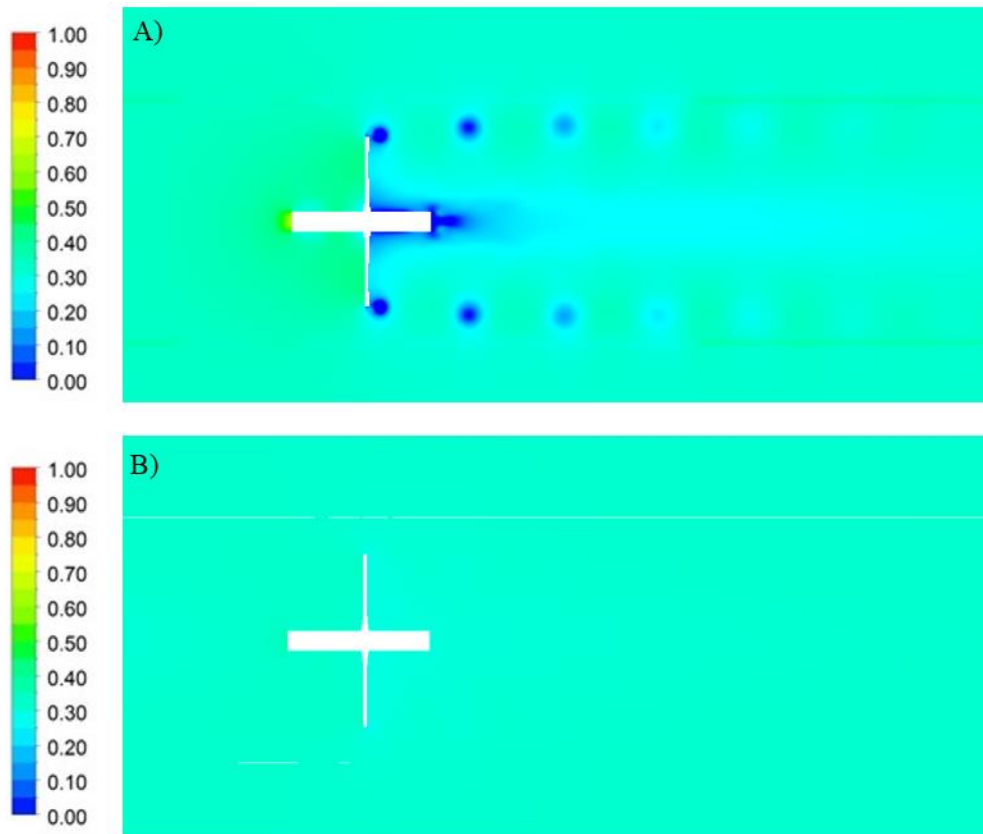
Figure 16. Instantaneous normalized static pressure contours for downstream unit in A) staggered and B) inline configuration with free-stream velocity of 2.25 m/s and constant rotation rate of 150 rpm
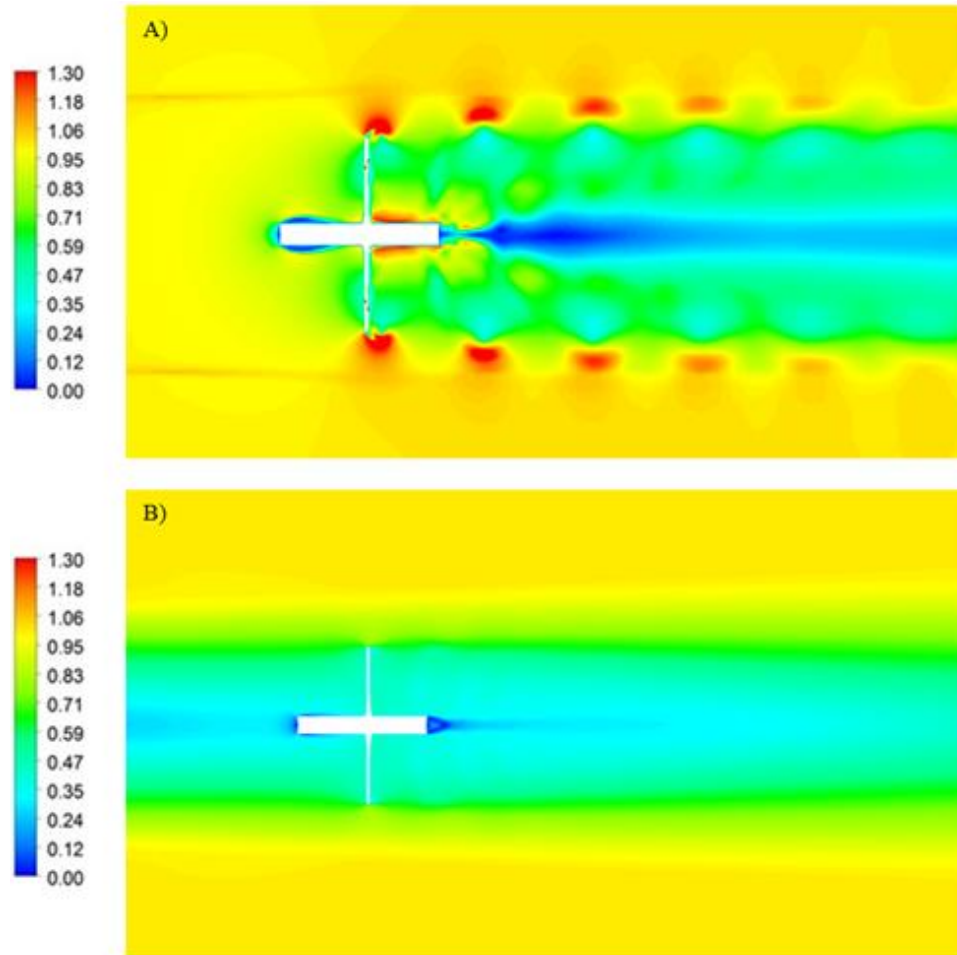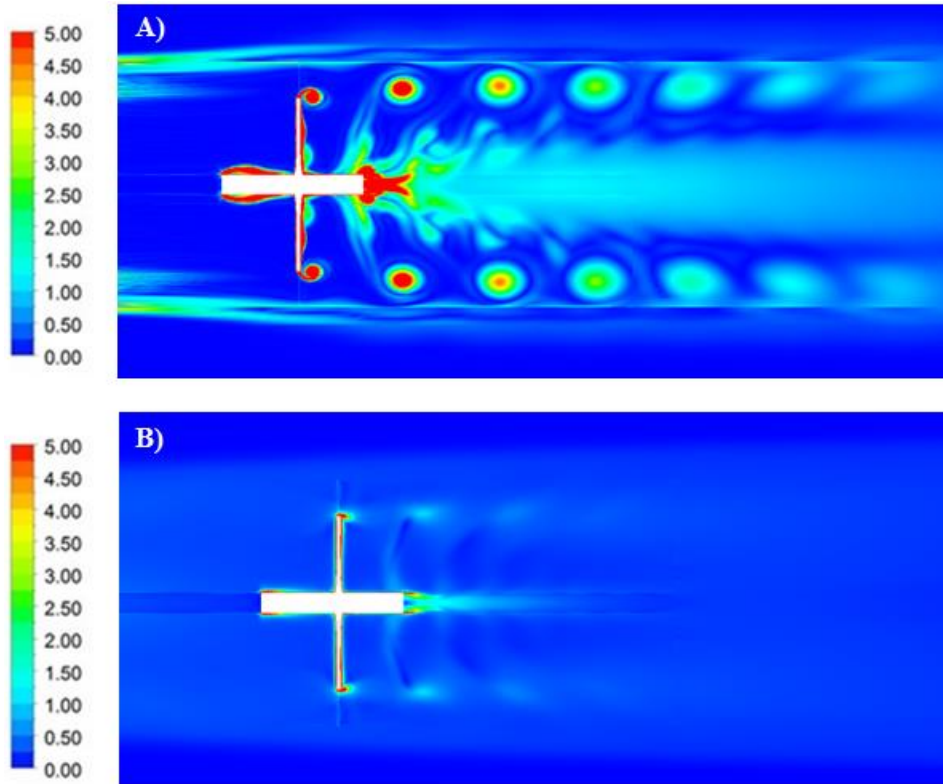
Figure 17. Instantaneous normalized vorticity contours for downstream unit in A) staggered and B) inline configuration with free-stream velocity of 2.25 m/s and constant rotation rate of 150 rpm.

4.2. Longitudinal Spacing Effect on Inline Downstream Turbine Performance

It is observed in previous section that the primary cause for inline-downstream unit performance reduction is low flow speed presenting within the wake region. Velocity magnitude in the wake region may be elevated by allowing flow to develop through increasing the spacing between units. In addition to constant stream-wise spacing, $6D_t$, an additional steady state simulation is conducted for $10D_t$ spacing. The relative power

37

obtained for both simulations are shown in Table 2. The increment in spacing from $6D_t$ to $10D_t$ enhanced relative power from 0.16 to 0.60.

Table 2. Relative Power Results for different spacing

Longitudinal Space	$6D_t$	$10D_t$
$\tilde{P}$ (Downstream Unit)	0.16	0.60

Figure 18 and Figure 19 depict normalized velocity and normalized vorticity contours of inline-downstream turbine respectively for the longitudinal spacing as $6D_t$ and $10D_t$. Velocity is normalized in the range of 0-1 instead of 0-1.3 applied within the previous contours in order to capture the flow field around turbine blade tip. The average velocity magnitude entering the downstream turbine is roughly 1.500 m/s and 1.661 m/s for the spacing of $6D_t$ and $10D_t$, respectively. This observation proves the reason of the increment in relative power for downstream turbine placed $10D_t$ away from the upstream unit. Furthermore, Figure 19 depicts more powerful tip vorticities for the unit placed within $10D_t$ longitudinal space.
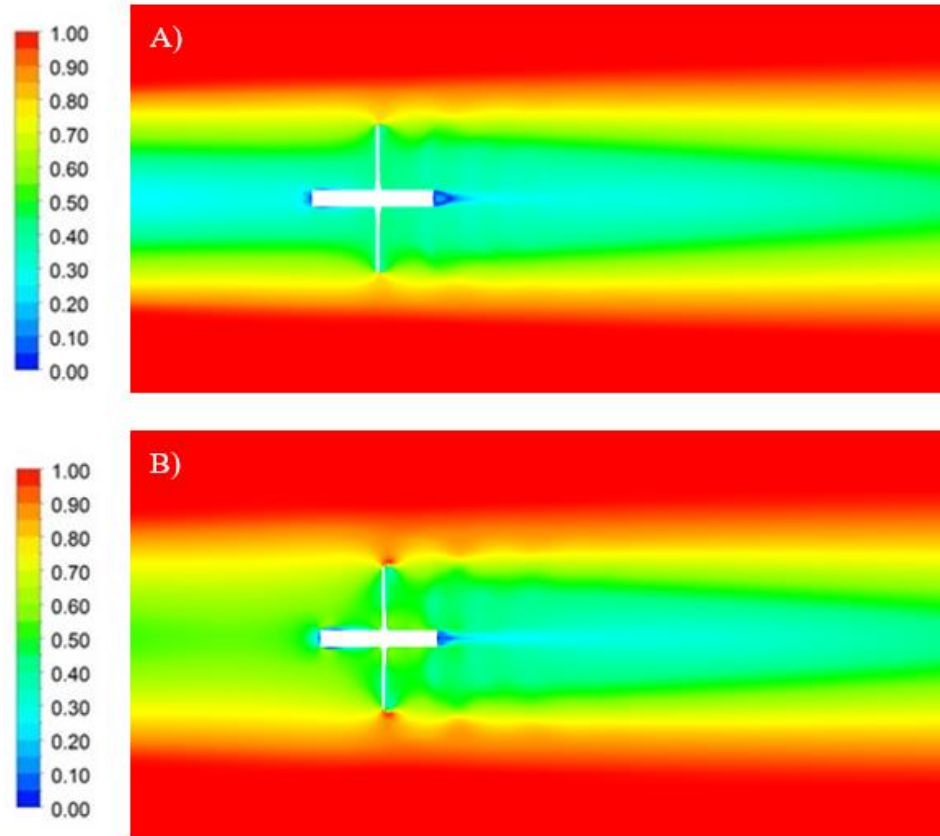
Figure 18. Normalized velocity contours of inline-downstream turbine for different longitudinal spacing as A) $6D_t$ and B) $10\boldsymbol{D_t}$ with free-stream velocity of 2.25 m/s and constant rotation rate of 150 rpm.
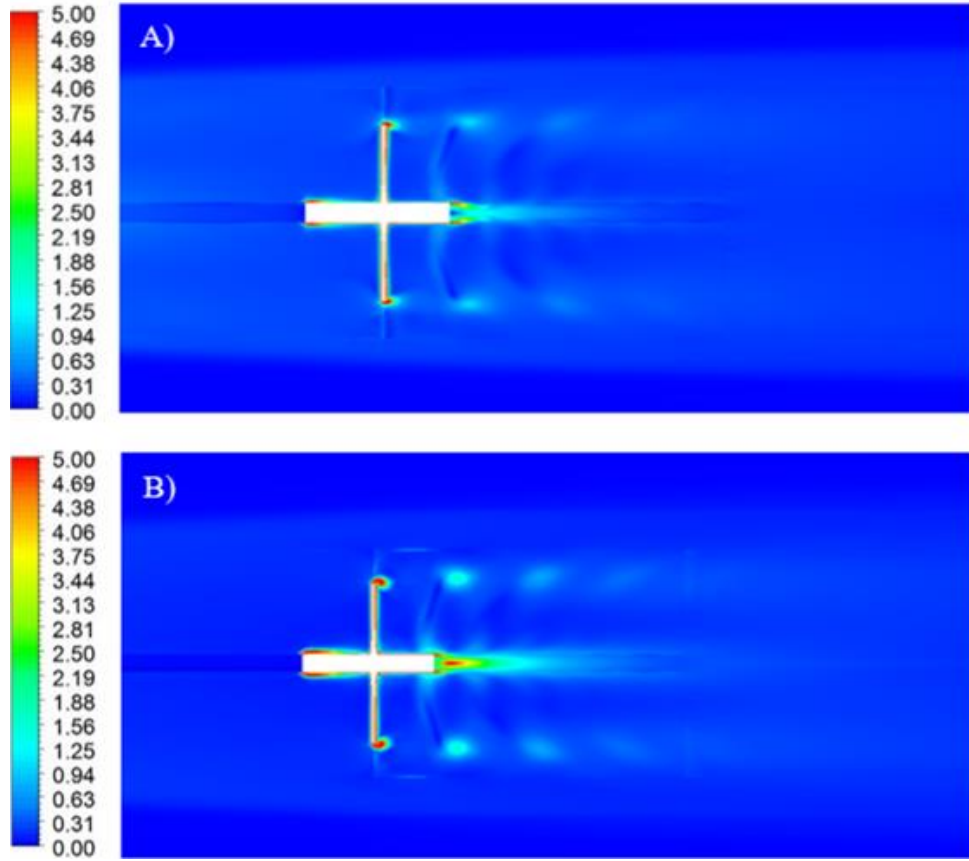
Figure 19. Normalized vorticity contours of inline-downstream turbine for different longitudinal spacing as A) $6D_t$ and B) $10D_t$ with free-stream velocity of 2.25 m/s and constant rotation rate of 150 rpm.

4.3. Rotation Speed Effect on Inline Downstream Turbine Performance

The turbine rotation speed and free stream velocity in previous sections was 150 rpm and 2.25 m/s, respectively. The free-stream speed of 2.25 m/s and rotation speed of 150 rpm yields tip speed ratio of 1.86 which corresponds to maximum power coefficient of 0.43 at Best Efficiency Point (BEP) as shown in $C_p - \lambda$ curve [9]. However, the incoming flow velocity for inline-downstream turbine drops significantly as a result of

wake region. The equation (22) proves that reduction in the flow velocity increases the tip speed ratio and decreases the power coefficient from BEP to a lower power coefficient. The first option to move power coefficient again to BEP is to decrease turbine rotation speed and the second solution is to design another turbine which has smaller rotor diameter.

In addition to 150 rpm constant rotation speed for downstream turbine, one more simulation was conducted by decreasing rotation speed to 100 rpm. Table 3 clarifies that changing rotation speed from 150 rpm to 100 rpm elevated relative power from 0.24 to 0.55 providing a 129% improvement by altering angular velocity. The average velocity magnitude entering downstream turbines is close to each other and they are roughly 1.552 m/s and 1.547 m/s for rotation speed of 150 rpm and 100 rpm, respectively.

Table 3. Relative Power Results for different rotation speed

Note: The computational domain is semi-circular shaped and side boundaries are **No-slip wall** instead of periodic boundary condition.

Rotation Speed	150 rpm	100 rpm
$\tilde{P}$ (Downstream Unit)	0.24	0.55

Normalized velocity and vorticity contours for inline downstream unit is depicted in Figure 20 and Figure 21 respectively for rotation speed of 150 rpm and 100 rpm. The tip vortices become more effective in the flow field for 100 rpm rotation speed. The reduction in turbine rotation speed resulted in lower velocity region in hub downstream

and more diffusive tip vortices around the turbine blade tips. The tip vorticity magnitude is higher for the lower rotation speed. This proves that the turbine interacts more within the flow field and this improves turbine performance at 100 rpm for the present flow parameters.

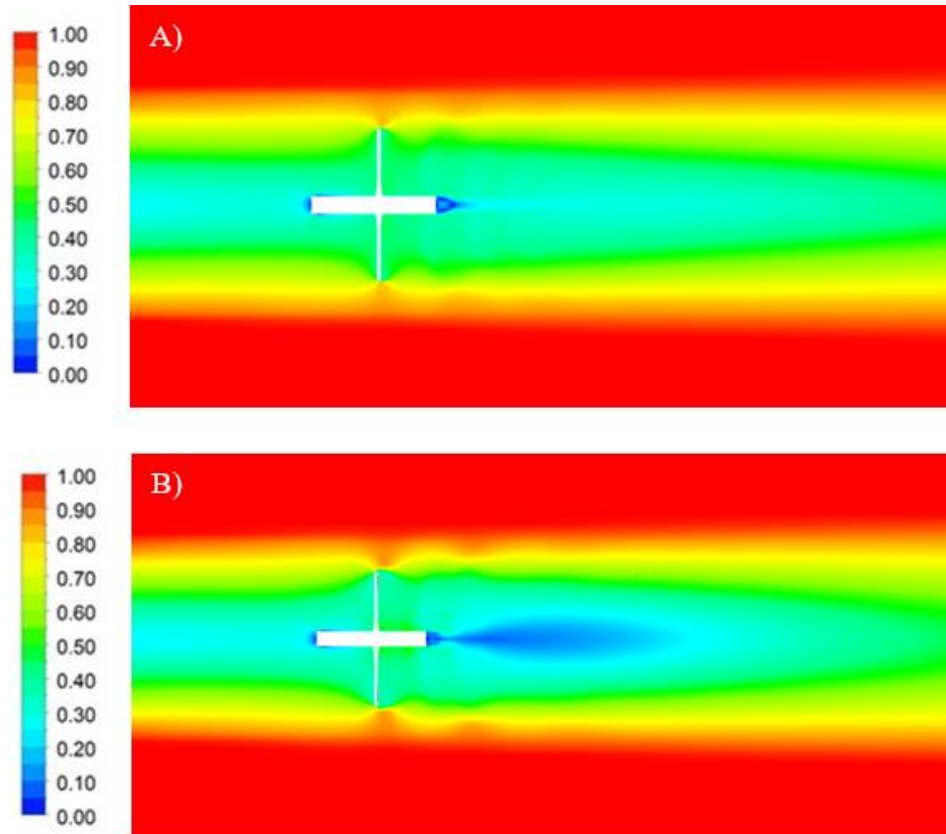Figure 20. Normalized velocity contours of inline-downstream turbine for different rotation speed as A) 150 rpm and B) 100 rpm with free-stream velocity of 2.25 m/s and longitudinal spacing of $6D_t$.
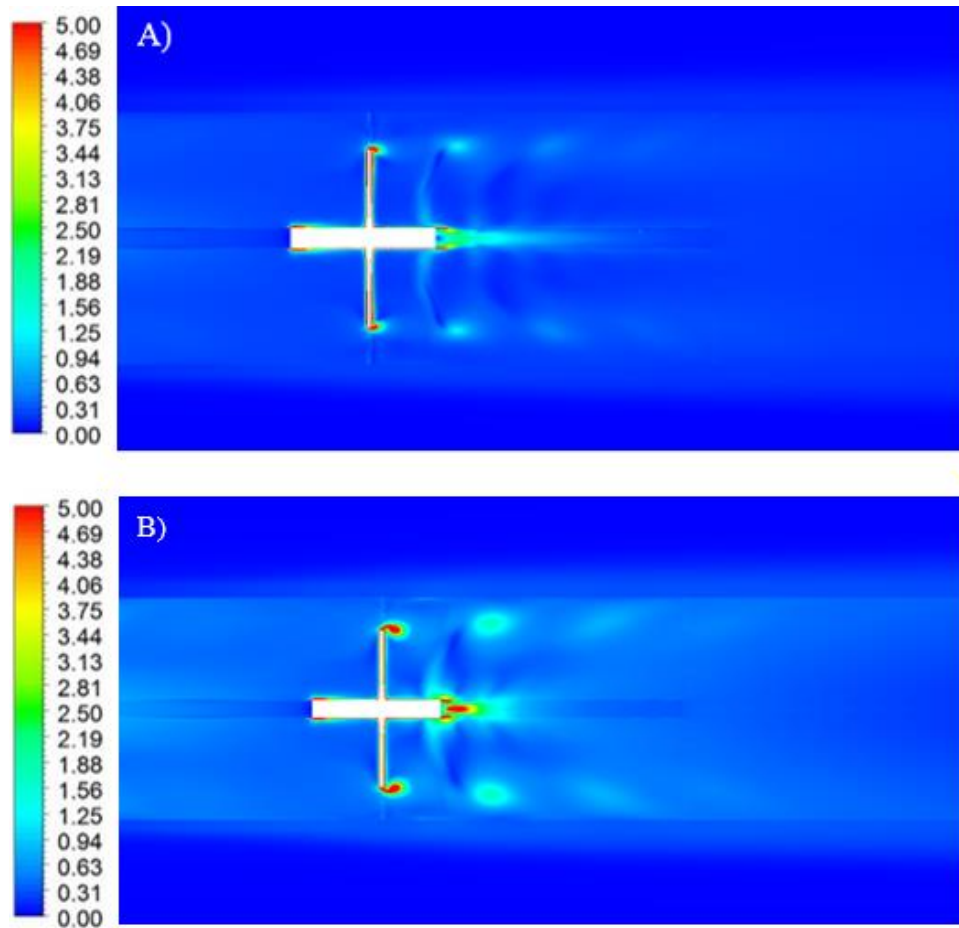
Figure 21. Normalized vorticity contours of inline-downstream turbine for different rotation speed as A) 150 rpm and B) 100 rpm with free-stream velocity of 2.25 m/s and longitudinal spacing of $6D_t$.

4. CONCLUSIONS

The steady state and transient CFD simulations were conducted for pre-designed, two-bladed hydrokinetic turbines documented by Schleicher *et al.* [9], present within the computational domain. Three bladed version of the present hydrokinetic turbine is optimized by Schleicher [10] and numerical predictions were validated experimentally by Riglin *et al.* [11, 12, 13]. Power coefficient measured for a single unit turbine agrees well with that predicted with a deviation of less than 3.0% at turbine optimum design point. The steady state and transient CFD simulations were conducted using ANSYS CFX for the present study. Inline and staggered configurations of two-turbine array were studied to determine the influence of wake interaction on turbine performance. For the inline configuration, the downstream unit performance is investigated using steady state analyses for various rotation rate and different stream-wise spacing between units.

The results showed that the steady state and the transient analyses yield nearly identical flow field and relative power. Upstream units in both inline and staggered configurations and the downstream unit in the staggered arrangement show a minimal deviation from predicted results of a single unit. However, the wake interaction behind the upstream turbine causes significant performance reduction for the downstream turbine and the relative power dropped to 0.18 for the inline configuration.

Further investigations are conducted to elevate the inline-downstream turbine performance by increasing the stream-wise spacing between the units and decreasing the turbine rotation rate. The incremental increase in longitudinal spacing from $6D_t$ to $10D_t$

enhances relative power from 0.16 to 0.60. Relative power of the downstream turbine is improved from 0.24 to 0.55.by lowering the rotation speed from 150 rpm to 100 rpm. This study will aid in designing and optimizing hydro farm consisting of multiple micro-hydrokinetic turbines operating in close proximity.

5. FUTURE STUDY

In reality, the computational domain for present study must include two phases as water and air to simulate free surface effect reliably. The air phase effect on turbine performance increases by turbine proximity to free surface. Therefore, to simplify the computations, the turbine is submerged deep enough to prevent free surface effects on turbine performance for the current study. The further research can be conducted to determine the free surface effect on multiple turbine performance.

Hydrokinetic turbines have a performance limit as named Betz Limit and hence the maximum performance coefficient for turbines without any surrounding structures is 0.593. Riglin *et al.* [28] conducted CFD simulations for single unit turbine by augmenting diffuser around the turbine rotor and concluded that the diffuser enhanced turbine power generation 48%. This enhancement in power generation motivates present study to conduct multiple array simulations with turbines diffuser augmented.

References

[1] Conti, J. J.; Holtberg, P. D.; Diefenderger, J. R.; Napolitano, S. A.; Schaal, A. M.; Turnure, J. T.; Westfall, L. D., "Annual Energy Outlook 2015 with Projections to 2040," U.S. Energy Information Administration, Washington, DC, 2015.

[2] Ravens, T.; Cunningham, K.; Scott, G., "Assessment and Mapping of the Riverrine Hydrokinetic Resource in the Continental United States," Electric Power Research Institude (EPRI), Palo Alto, CA, 2012.

[3] "U.S. Geological Survey, National Wayer Information System," 2014. [Online]. Available: http://waterdata.usgs.gov/nwis/.

[4] Jo, C. H., Lee, K. H., Lee, J. H., Nichita, C., "Multi-arrayed tidal current energy farm and the integration method of the power transportation," in *Power Electronics, Electrical Drives, Automation and Motion (SPEEDAM), 2012 International Symposium on*, 2012.

[5] Malki, R., Masters, I., Williams, A. J., & Croft, T. N., "Planning tidal stream turbine array layouts using a coupled blade element momentum–computational fluid dynamics model," *Renewable Energy,* vol. 63, pp. 46-54, 2014.

[6] Mycek, P., Gaurier, B., Germain, G., Pinon, G., Rivoalen, E., "Experimental study of the turbulence intensity effects on marine current turbines behaviour. Part II: Two interacting turbines," *Renewable Energy,* vol. 68, pp. 876-892, 2014.

[7] Gebreslassie, M. G., Belmont, M. R., Tabor, G. R., "Comparison of Analytical and CFD Modelling of the Wake Interactions of Tidal Turbines.," in *10th European Wave and Tidal Energy Conference (EWTEC2013)*, Aalborg, Denmark, 2013.

[8] Churchfield, M. J., Li, Y., Moriarty, P. J., "A large-eddy simulation study of wake propagation and power production in an array of tidal-current turbines," in *9th European Wave and Tidal Energy Conference (EWTEC2009)*, Southampton, UK, 2011.

[9] Schleicher, W. C., Riglin, J. D., Oztekin, A., "Numerical characterization of a preliminary portable micro-hydrokinetic turbine rotor design," *Renewable Energy,* vol. 76, pp. 234-241, 2015.

[10] W. C. Schleicher, "Design Optimization of a Portable, Micro-hydrokinetic Turbine," Bethlehem, 2015.

[11] Riglin, J., Carter III, F., Oblas, N., Schleicher, W. C., Daskiran, C., Oztekin, A., "Experimental and Numerical Characterization of a Full-Scale Portable Hydrokinetic Turbine Prototype for River Applications," *Renewable energy, Manuscript submitted for publication.*

[12] J. Riglin, "Design, Modeling, and Prototyping of a a Hydrokinetic Turbine Unit for River Application," Bethlehem, 2016.

[13] Riglin, J., Daskiran, C., Oblas, N., Schleicher, W. C., Oztekin, A., "Design and Characteristics of the Micro-Hydrokinetic Turbine System," in *ASME 2015 International Mechanical Engineering Congress and Exposition*, Houston, Texas, 2015.

[14] "Interfaces, Sources and Additional Variables," 2009.

[15] F. R. Menter, "Two-Equation Eddy-Viscosity Turbulence Models for Engineering Applications," *AIAA Journal,* vol. 32, no. 8, pp. 1598-1605, 1994.

[16] F. R. Menter, "Zonal Two-Equation k-ω Turbulence Models for Aerodynamic Flows," *AIAA Paper 93-2906.*

[17] Menter, F. R., Kuntz, M., Langtry, R., "Ten years of industrial experience with the SST turbulence model," *Turbulence, heat and mass transfer 4(1),* 2003.

[18] "Fluent 12 Theory Guide," 2009.

[19] T. J. Hall, "Numerical simulation of a cross flow marine hydrokinetic turbine," 2012.

[20] "Fluent 6.3 User's Guide," 2006.

[21] P. J. Roache, "A method for uniform reporting of grid refinement studies," in *Proceedings of the 11th AIAA Computational Fluid Dynamics Conference*, Orlando, 1993.

[22] P. J. Roache, "Perspective: a method for uniform reporting of grid refinement studies," *ASME Journal of Fluids Engineering,* vol. 116, no. 3, pp. 405-413, 1994.

[23] P. J. Roache, "Quantification of Uncertainty in Computational Fluid Dynamics," *Annual Review of Fluid Mechanics,* vol. 29, pp. 123-160, 1997.

[24] Celik, I.; Chen, C. J.; Roache, P. J.; Scheurer, G., "Symposium on Quantification of Uncertainty in Computational Fluid Dynamics," in *FED-ASME*, New York, 1993.

[25] J. D. Anderson, Computational fluid dynamics : the basics with applications, McGraw Hill International , 1995.

[26] Daskiran, C., Riglin, J., Oztekin, A., "Computational Study of Multiple Hydrokinetic Turbines: The Effect of Wake," in *ASME 2015 International Mechanical Engineering Congress and Exposition*, Houston, Texas, 2015.

[27] Riglin, J., Daskiran, C., Schleicher, W., Oztekin, A., "Transient Analysis of Micro-Hydrokinetic Turbines for River Applications," *Ocean Engineering, Manuscript submitted for publication.*

[28] Riglin, J., Schleicher, W. C., Oztekin, A., "Diffuser Optimization for a Micro-Hydrokinetic Turbine," in *ASME 2014 International Mechanical Engineering Congress and Exposition*, Montreal, Canada, 2014.

Vita

Cosan Daskiran was born on March 22, 1990 to Erol and Aynur Daskiran in Zonguldak, Turkey. He graduated from Zonguldak Ataturk Anatolian High School in 2008 by the first position in science with the degree of 95.31 of 100 and then he attended Istanbul Technical University (ITU) for his Bachelor degree.

His undergraduate education has given him a certain set of skills and strong fundamentals in Mechanical Engineering to take part in different projects in several fields. He graduated from Mechanical Engineering Department of ITU in February, 2012 with a GPA of 3.14.

After the completion of his Bachelor Science in Turkey, Cosan started his graduate program at Mechanical Engineering Department at Lehigh University in August, 2013.